ChemComm

COMMUNICATION

Check for updates

Zn-flux-enabled synthesis of orthorhombic kagome YbFe$_6$Ge$_6$: Yb reduction and magnetic behavior

Rahul Meduri,[a] Grant R. Wilkinson,[b] Muhammad Z. Idrees,[c] Kaya Wei, [ID][d]
Sebastian A. Stoian, [ID][c] Henry S. La Pierre, [ID][b] Gregory T. McCandless[a] and
Julia Y. Chan [ID] *[a]

Single crystals of an orthorhombic polymorph of kagome metal YbFe$_6$Ge$_6$ were grown from Zn flux. This Zn-flux-stabilized phase exhibits mixed Yb valency and magnetic behavior that differs from its hexagonal counterpart, underscoring the profound influence of flux selection on both structure and physical properties in intermetallic materials.

Flux growth synthesis is an efficient method for producing bulk single-crystalline materials.[1,2] The technique not only enables the discovery of compounds within complex phase spaces, but also facilitates the growth of large single crystals suitable for physical measurements. Flux growth leverages eutectic points in a mixture of elements, often utilizing a low-melting metal or compound to reduce the overall melting point of a reaction. The technique permits synthesis with refractory elements to be more accessible, thus making it particularly valuable for the exploratory growth of intermetallic phases. Conventional synthesis methods for intermetallic compounds typically promote the formation of thermodynamically stable phases within a given composition space, thereby limiting access to metastable or otherwise unexplored structural regions that require kinetic or non-equilibrium control.[3] Flux growth can circumvent this by altering reaction pathways through adjustable experimental parameters intrinsic to the technique. For example, the formation of specific products can be guided by tuning the cooling rate or by selecting the temperature at which the reaction is removed from the furnace and the excess flux is removed. This level of control was demonstrated through the investigation of the Ce–Pd–Ga phase space where the use excess Ga flux lead to the discovery of a family of structurally related compounds.[2,4] A range of related structures were obtained by tuning the heating parameters, which illustrate the diverse parametric control of flux growth methods. In the synthesis of the Pr$_{n+1}$Co$_n$Ge$_{3n+1}$ homologous series,[5] the concentration of flux used directly affected which n-members and related phases crystallized from the melt. This study reinforced the notion that flux concentration itself serves as a valuable tuning parameter for directing phase formation.[6] Harnessing control over structural formation within a phase space is also evident in the stabilization of the two polymorphs of Pr$_2$Co$_3$Ge$_5$, one orthorhombic[7] and one monoclinic, the latter displaying nearly Pr^{4+} character, which is rare for Pr intermetallic compounds.[8]

In this communication, we demonstrate how the choice of flux can decisively influence phase formation in intermetallic synthesis. YbFe$_6$Ge$_6$ is a member of the broader family of rare-earth kagome metals.[9,10] The HfFe$_6$Ge$_6$-type structure (h-YbFe$_6$Ge$_6$, SG: $P6/mmm$) is routinely grown from a Sn flux and hosts a low temperature spin reorientation near 63 K,[11,12] a feature associated with an anomalous Hall effect.[13] The Y$_{0.5}$Co$_3$Ge$_3$-type structure (y-YbFe$_6$Ge$_6$, SG:$P6/mmm$) can also be obtained through conventional arc-melting and annealing at 900 °C and does not possess the spin reorientation present in the ordered variant.[14] Here, we show that loading Yb, Fe, Ge with an excess of Zn flux, yields an orthorhombic polymorph of YbFe$_6$Ge$_6$ (o-YbFe$_6$Ge$_6$, SG: $Cmcm$) that adopts the TbFe$_6$Sn$_6$ structure type and, exhibits differing magnetic properties than its hexagonal counterpart. Energy-dispersive X-ray spectroscopy confirms Zn incorporation into the structure while powder diffraction indicates a preferential Zn site occupation within the Fe-based kagome slabs (Fig. S2). For simplicity, we refer to Zn-flux-stabilized orthorhombic phase, YbFe$_{5.52}$Zn$_{0.48}$Ge$_6$, as o-YbFe$_6$Ge$_6$ throughout this communication. Single crystals of o-YbFe$_6$Ge$_6$ were grown out of excess Zn flux with sizes up to 5 mm, adopting a hexagonal prism morphology (Fig. S1, inset). Synthesis conditions and structure determination using powder X-ray diffraction, single crystal X-ray diffraction and energy dispersive X-ray spectroscopy are provided in the SI.

[a] Department of Chemistry and Biochemistry, Baylor University, Waco, TX, 76798, USA. E-mail: Julia_Chan@baylor.edu

[b] School of Chemistry and Biochemistry, Georgia Institute of Technology, Atlanta, GA, 30332, USA

[c] Department of Chemistry, University of Idaho, Moscow, ID, 83844, USA

[d] National High Magnetic Field Laboratory, Tallahassee, FL, 32310, USA

Fig. 1 shows the unit cell of o-YbFe$_6$Ge$_6$ (a) and the pattering scheme of the Yb sublattice (b). Crystallographic data and refinement parameters for o-YbFe$_6$Ge$_6$ are given in Table S2 and atomic coordinates of o-YbFe$_6$Ge$_6$ are given in Table S3. Crystallographic comparison with h-YbFe$_6$Ge$_6$ was performed using the CIF from our previous report, as the reactant stoichiometry offers a more meaningful comparison to the orthorhombic variant under similar synthesis conditions.[15] Both the h-YbFe$_6$Ge$_6$ and o-YbFe$_6$Ge$_6$ structures consist of alternating honeycomb and kagome slabs that are stacked in a staggered fashion, forming channels which house the Yb and the Ge–Ge dimer (Fig. S3a and b). In h-YbFe$_6$Ge$_6$, Yb occupies every other honeycomb slab along the c-axis. Structural complexity increases in o-YbFe$_6$Ge$_6$ due to differences in Yb ordering, which represents the main feature of distinction between the two structure types. Assuming the absence of the disordered sites, in h-YbFe$_6$Ge$_6$, the Yb atoms centered within the honeycomb hexagons are adjacent to one another in the ab plane. In contrast, o-YbFe$_6$Ge$_6$ exhibits a staggered Yb arrangement along the b-axis, such that every other pair of Yb atoms is adjacent. Unlike h-YbFe$_6$Ge$_6$, where Yb occupies every other honeycomb layer along the c-axis, the orthorhombic variant possesses Yb in each honeycomb layer along the a-axis, resulting in a more intricate ordering scheme. The reason behind the specific ordering was discussed in detail by Fredrickson et al.[16] It is seen that with larger rare earth elements occupying the hexagons of the honeycomb layer (or other constituent elements that surround the rare earth), they are increasingly unable to order adjacent to one another because of increased steric interactions, leading to a staggered ordering of the rare

earth element. One detour from the hexagonal to orthorhombic transition is seen with the hexagonal Y$_{0.5}$Co$_3$Ge$_3$ structure type; that harbors large amounts of positional disorder of Yb and Ge dimers, resulting in a reduction of the hexagonal HfFe$_6$Ge$_6$-type cell by $c/2$. Our previous report of Yb$_{0.5}$(Co$_{1-x}$Fe$_x$)$_3$Ge$_3$ explores the structural transition from a Y$_{0.5}$Co$_3$Ge$_3$/CoSn hybrid structure to the HfFe$_6$Ge$_6$ structure type as a function of Fe substitution.[15]

Fig. S4c and d show the honeycomb sublattice of the h-YbFe$_6$Ge$_6$ and o-YbFe$_6$Ge$_6$ structures, respectively with distinct interatomic distances highlighted to show how the perfect hexagonal slab in the h-YbFe$_6$Ge$_6$ structure differs from the irregular hexagons present in o-YbFe$_6$Ge$_6$. Fig. S4e and Fig. S4f show the areas of the h-YbFe$_6$Ge$_6$ and o-YbFe$_6$Ge$_6$ hexagons, respectively. Fig. S3c and d show the patterning scheme of the Ln environment in h-YbFe$_6$Ge$_6$ and o-YbFe$_6$Ge$_6$ which differs based on the occupancy of the lanthanide in the honeycomb net. Using the rationale that unfavorable steric environments can drive an orthorhombic distortion, we propose that Zn incorporation on the Fe sites reduces the local volume surrounding the Yb atoms in a manner reminiscent trends in of our previous doping study.[15] Another possibility we considered is that Yb in o-YbFe$_6$Ge$_6$ may not be strictly trivalent; partial Yb^{2+} character could increase the average ionic radius and therefore influence the observed structural distortion. We also note that differences in synthesis conditions between h-YbFe$_6$Ge$_6$ and o-YbFe$_6$Ge$_6$ may play a role. Synthesis-dependent polymorphism has been documented in YFe$_6$Sn$_6$ and DyFe$_6$Sn$_6$,[17] and studies of FeGe also previously showed that the annealing conditions affected the structural ordering,[18] thus in our Yb$_{0.5}$(Co$_{1-x}$Fe$_x$)$_3$Ge$_3$ report, an annealing step of 72 h was performed to ensure structural consistency in the doped series; such post-growth annealing was not performed here. When attempting to use the same heating profile as our previous report, the orthorhombic polymorph consistently forms with the only difference in structure being the amount of positional disorder present, which could be due to either the change in cooling rate or the time dwelled.

X-ray absorption spectroscopy (XAS) performed at the Yb L_3-edge was used to quantify the Yb oxidation state in o-YbFe$_6$Ge$_6$ (see SI for measurement details). The resulting normalized spectra for o-YbFe$_6$Ge$_6$ and the known +3 oxidation state reference YbCl$_3$ are shown in Fig. 2. Measurement of the edge energy via derivative analysis (Fig. S5c), reveals a small redshift in the edge energy from 8944.11 eV for YbCl$_3$ to 8942.68 eV for o-YbFe$_6$Ge$_6$ ($\Delta E = -1.43$ eV) consistent with an oxidation state assignment Yb^{3+} for the YbFe$_6$Ge$_6$ analyte.[19] In addition to this main feature, the derivative of the spectrum displayed an additional, lower energy feature that contributes to the broad nature of the primary peak. Peak fitting analysis (see SI) was performed to deconvolute the spectrum. This revealed a secondary, lower intensity peak centered at 8938.27(5) eV, redshifted ~ 6.6 eV from the main peak at 8944.846(16) eV. While the higher energy peak is consistent with Yb^{3+}, the lower energy peak is consistent with a small percentage of Yb^{2+} character in the compound and this intermediate-valence effect has been
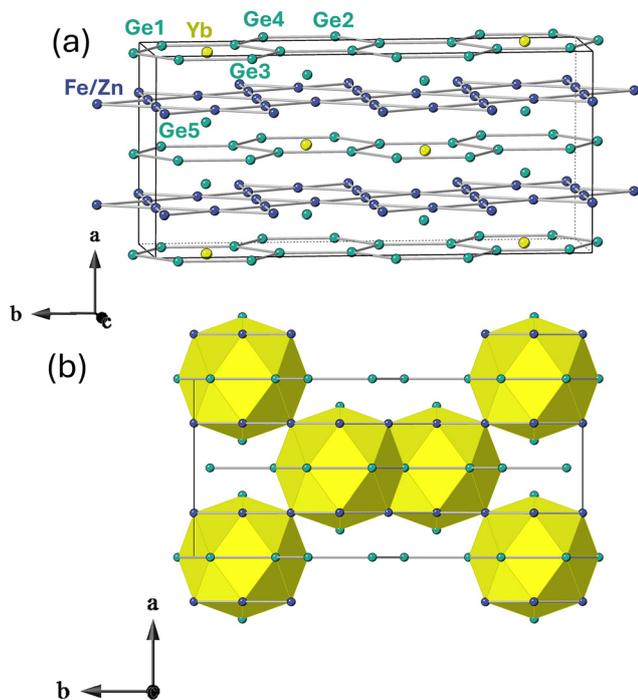

Fig. 1 Unit cell (a) and pattering scheme (b) along the b-direction of o-YbFe$_6$Ge$_6$, disordered sites omitted for clarity.
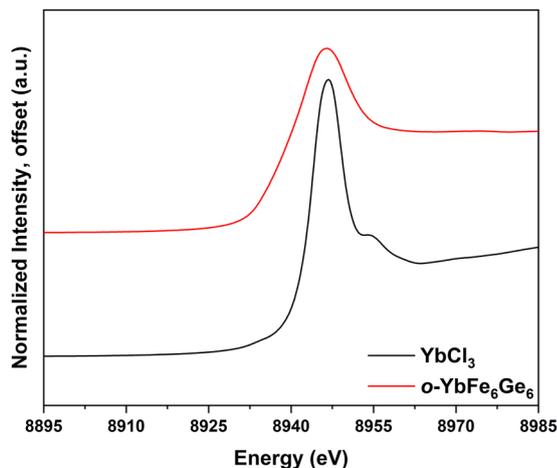
Fig. 2 Normalized (offset) Yb L_3-edge spectra for $YbCl_3$ (black) and o-$YbFe_6Ge_6$ (red).

observed in other Yb-containing intermetallic compounds.[20–23] The appearance of Yb^{2+} character in these systems is associated with coupling of the conduction band electrons to the $4f$ hole of Yb^{3+}, which itself lies near the Fermi energy. The increase of valency in the kagome sublattice with Zn substitution can also be contributing to the reduction of Yb. To estimate the relative $Yb^{2+/3+}$ character of o-$YbFe_6Ge_6$, the ratio of the peak area of the Yb^{3+} feature to the sum of the area of both peaks, denoted n_f (eqn (S1)), is calculated and found to be 0.79(8), which is consistent with the assignment of a formal Yb^{3+} oxidation state, with relatively minor amounts of Yb^{2+} character and an effective oxidation state (eqn (S2)) of +2.79(8) at the measurement temperature of 7 K.

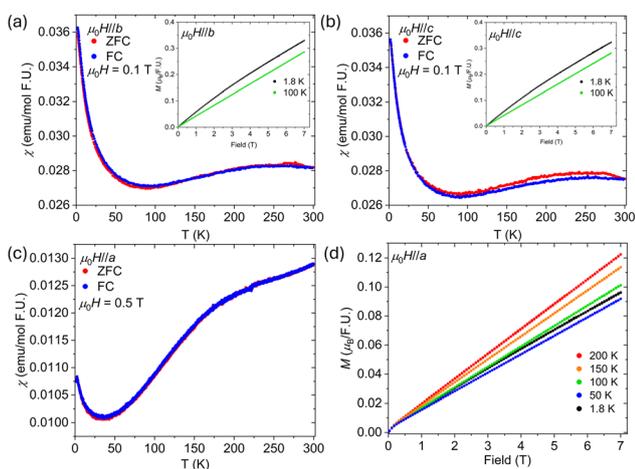Fig. 3a and b presents the anisotropic temperature-dependent magnetic susceptibility measurements when the applied

Fig. 3 Temperature-dependent magnetic susceptibility of o-$YbFe_6Ge_6$ where (a) $\mu_0H\|b$ and (b) $\mu_0H\|c$. The inset of both plots is the field-dependent magnetization data up to 7 T at 100 K and 1.8 K isotherms. (c) Temperature-dependent magnetic susceptibility where $\mu_0H\|a$. (d) Field-dependent magnetization up to 7 T at 200 K, 150 K, 100 K, 50 K, and 1.8 K where $\mu_0H\|a$.

magnetic field is parallel to the b-direction and c-direction ($\mu_0H\|b$ and $\mu_0H\|c$), respectively. The data for both field orientations are largely comparable, showing a broad hump beginning near 300 K, which suggests possible spin canting or fluctuations of the Fe moments down to approximately 100 K, where the emergence of Yb paramagnetism becomes apparent. The magnetization *versus* applied magnetic field measurements (inset) at $T = 100$ K and $T = 1.8$ K also exhibit similar behavior, characterized by an almost linear field dependence. These similarities for fields applied parallel to the b- and c-directions can be attributed to the fact that in both cases the field lies parallel to the kagome planes. Fig. 3c and d present the temperature-dependent magnetic susceptibility and the field-dependent magnetization, respectively, when the field is applied parallel to the a-direction ($\mu_0H\|a$). The susceptibility exhibits a gradual decrease from 300 K to about 50 K where a paramagnetic upturn is observed. Field-dependent magnetization measurements were collected at several temperatures to examine how changes in magnetic field strength influence the downturn observed in the magnetic susceptibility. The 200 K isotherm exhibits the largest magnetization across the measured field range. As the temperature decreases, the overall magnetization systematically diminishes until 50 K, where the onset of the Yb paramagnetic contribution becomes apparent, consistent with the susceptibility data. At 1.8 K, the magnetization increases slightly relative to the 50 K isotherm, reflecting the growing Yb paramagnetism at low temperatures. $LnFe_6Ge_6$ members (Ln = Gd-Lu) adopt an antiferromagnetic ordering of Fe moments along the kagome stacking axis at approximately 480–490 K.[9] In compounds adopting the $HfFe_6Ge_6$ structure type, this axis corresponds to the c-axis, whereas in those with the $TbFe_6Sn_6$ structure type, it corresponds to the a-axis (Fig. 1). Therefore, in o-$YbFe_6Ge_6$ ($TbFe_6Sn_6$-type), the a-axis can be considered the magnetic "hard axis," consistent with the orientation of the antiferromagnetically ordered Fe moments. Direct confirmation of the Fe-sublattice magnetic transition would require high-temperature magnetic susceptibility measurements, as the transition is expected to occur well above room temperature. This interpretation is further supported by the reduced magnitude of the susceptibility for $\mu_0H\|a$ compared to $\mu_0H\|b$ and $\mu_0H\|c$. Reliable Curie–Weiss fits could not be obtained because the Fe sublattice likely orders above 300 K, preventing access to a true paramagnetic regime for the Fe moments. The paramagnetic upturn observed below ~50 K is attributed to the emergence of localized Yb^{3+} moments, which begin to dominate the magnetic response as thermal fluctuations decrease. At higher temperatures, the broad behavior of the magnetic susceptibility is governed primarily by Fe-based interactions, potentially involving weak spin canting or short-range correlations within the kagome planes. This is most likely a result of Zn incorporation into the Fe lattice, which diminishes the long-range ordering normally exhibited in a pure Fe kagome slab. As the temperature decreases, the Yb^{3+} ions display Curie–Weiss-like behavior, producing the rapid increase in susceptibility. This temperature evolution reflects a crossover from itinerant Fe magnetism at high temperatures to localized rare-earth paramagnetism at low temperatures,
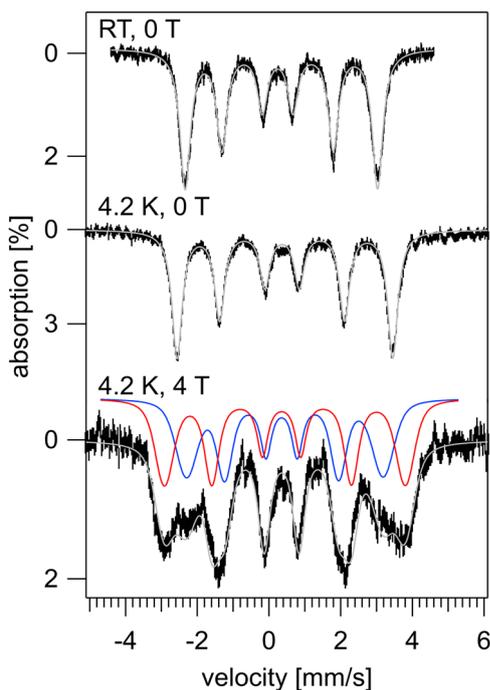
Fig. 4 ^{57}Fe Mössbauer spectra recorded for o-YbFe$_6$Ge$_6$, see text. The solid grey traces are theoretical spectra obtained using the parameters listed in Table S4. The theoretical 4 T spectrum was obtained from the sum of two components shown in blue and red above the experimental data.

consistent with the onset of Yb-moment polarization in applied magnetic fields.

The temperature dependent, zero-field ^{57}Fe Mössbauer spectra recorded for o-YbFe$_6$Ge$_6$ exhibit a single well defined six-line pattern, see Fig. 4 and Fig. S7. These spectra demonstrate that there is a spontaneous magnetic field acting on the ^{57}Fe nuclei which reveals that the iron sublattice is magnetically ordered. Inspection of Fig. 4, Fig. S8, and Table S4 shows that the hyperfine field increases from B_{eff} = 16.6 T at room temperature to 18.6 T at 4.2 K. These values are $\sim$10% larger than those reported for h- and y-type YbFe$_6$Ge$_6$.[11,14,24,25] Assuming that the 11.39 T μ_B^{-1} conversion factor determined at 150 K for h-YbFe$_6$Ge$_6$ from its combined neutron diffraction and ^{57}Fe Mössbauer spectroscopic investigation is still valid, these values suggests that for o-YbFe$_6$Ge$_6$ the iron-based magnetic moment increases from 1.46μ_B at room temperature to 1.63μ_B at 4.2 K. Importantly, lowering the temperature below 80 K does not lead to a broadening or a splitting of the observed resonances. This indicates that, just like for y-YbFe$_6$Ge$_6$, the spin reorientation transition observed at $\sim$63 K for h-YbFe$_6$Ge$_6$ is suppressed by the increased disorder of the Yb sites. Field dependent data up to 8 T was also collected (Fig. S9). These spectra suggest that above 6 T, the onset of a metamagnetic transition may occur even with no obvious features in the magnetization.

Several factors may account for the differences in magnetic behavior. (1) In the h-YbFe$_6$Ge$_6$ polymorph, XAS measurements confirm that Yb is trivalent. However, it is seen here that the o-YbFe$_6$Ge$_6$ polymorph has mixed valency that could potentially alter Yb–Fe coupling. (2) Partial substitution of Fe by Zn within the kagome lattice suppresses magnetic exchange among Fe atoms, thereby weakening the Yb–Fe coupling through alloy dilution. (3) The magnetic distinctions may also arise from differences in the structural ordering of the Yb sublattice. h-YbFe$_6$Ge$_6$ features a well-ordered triangular arrangement of Yb atoms, while the highly disordered y-YbFe$_6$Ge$_6$ contains a random Yb distribution and is reported to lack the spin reorientation present in the ordered variant.[14] The specific patterning scheme of Yb atoms we observe in o-YbFe$_6$Ge$_6$ may similarly disrupt Yb-Fe exchange interactions. Given that the temperature dependent Mössbauer spectra manifests similar behavior as the y-YbFe$_6$Ge$_6$, the origin in the differences in magnetism seem to strongly point to the pattern of the Yb sublattice. In conclusion, the reduction of Yb from a Zn flux growth leads to a change in physical properties and structure in o-YbFe$_6$Ge$_6$ when compared to the previously reported h-YbFe$_6$Ge$_6$. Clarifying the mechanism of growth and its influence on the contrasting physical properties of h-YbFe$_6$Ge$_6$ and o-YbFe$_6$Ge$_6$ will require the use of *in situ* diffraction and spectroscopic methods and are a prospect of future work. The present study underscores the critical role of parametric control of the flux growth method as well as its significance in enabling the synthesis of previously inaccessible phases.

Conflicts of interest

There are no conflicts to declare.

Data availability

The data supporting this article are included as part of the supplementary information (SI). Supplementary information: additional experimental details, XRD, crystallographic data, XAS analysis, and additional Mössbauer spectra. See DOI: https://doi.org/10.1039/d6cc00958a.

CCDC 2528289 contains the supplementary crystallographic data for this paper.[26]

Acknowledgements

References

1 P. C. Canfield and Z. Fisk, Growth of Single Crystals From Metallic Fluxes, *Philos. Mag. B*, 1992, **65**, 1117–1123.

2 W. A. Phelan, M. C. Menard, M. J. Kangas, G. T. McCandless, B. L. Drake and J. Y. Chan, Adventures in Crystal Growth: Synthesis and Characterization of Single Crystals of Complex Intermetallic Compounds, *Chem. Mater.*, 2012, **24**, 409–420.

3 M. G. Kanatzidis, R. Pöttgen and W. Jeitschko, The Metal Flux: A Preparative Tool for the Exploration of Intermetallic Compounds, *Angew. Chem., Int. Ed.*, 2005, **44**, 6996–7023.

4 S. E. Latturner, Clusters, Assemble: Growth of Intermetallic Compounds from Metal Flux Reactions, *Acc. Chem. Res.*, 2018, **51**, 40–48.

5 T. M. Kyrk, M. Bravo, G. T. McCandless, S. H. Lapidus and J. Y. Chan, Investigating the $A_{n+1}BnX_{3n+1}$ Homologous Series: A New Platform for Studying Magnetic Praseodymium Based Intermetallics, *ACS Omega*, 2022, **7**, 19048–19057.

6 T. M. Kyrk, M. G. Anderson, G. T. McCandless, S. H. Lapidus and J. Y. Chan, Influence of ''Non-Interacting'' Flux Concentration in Metallic Flux Growth Synthesis, *Chem. Mater.*, 2025, **37**, 2603–2610.

7 T. M. Kyrk, E. R. Kennedy, J. Galeano-Cabral, K. Wei, G. T. McCandless, M. C. Scott, R. E. Baumbach and J. Y. Chan, Anisotropic Magnetic and Transport Properties of Orthorhombic o-$Pr_2Co_3Ge_5$, *J. Phys.: Mater.*, 2022, **5**, 044007.

8 T. M. Kyrk, E. R. Kennedy, J. Galeano-Cabral, G. T. McCandless, M. C. Scott, R. E. Baumbach and J. Y. Chan, Much More to Explore with an Oxidation State of Nearly Four: Pr Valence Instability in Intermetallic m-$Pr_2Co_3Ge_5$, *Sci. Adv.*, 2024, **10**, eadl2818.

9 G. Venturini, R. Welter and B. Malaman, Crystallographic Data and Magnetic Properties of RT_6Ge_6 compounds (R = Sc, Y, Nd, Sm, Gd-Lu; T = Mn, Fe), *J. Alloys Compd.*, 1992, **185**, 99–107.

10 G. Venturini, Filling the CoSn Host-Cell: The $HfFe_6Ge_6$-type and the Related Structures, *Z. Kristallogr. - New Cryst. Struct.*, 2006, **221**, 511–520.

11 T. Mazet and B. Malaman, Evidence of Spin Reorientation in $YbFe_6Ge_6$ from Neutron Diffraction and ^{57}Fe Mössbauer Experiments, *J. Phys.: Condens. Matter*, 2000, **12**, 1085–1095.

12 M. A. Avila, T. Takabatake, Y. Takahashi, S. L. Bud'ko and P. C. Canfield, Direct Observation of Fe spin Reorientation in Single-Crystalline $YbFe_6Ge_6$, *J. Phys.: Condens. Matter*, 2005, **17**, 6969–6979.

13 W. Yao, S. Liu, H. Kikuchi, H. Ishikawa, Ø. S. Fjellvåg, D. W. Tam, F. Ye, D. L. Abernathy, G. D. A. Wood, D. Adroja, C.-M. Wu, C.-L. Huang, B. Gao, Y. Xie, Y. Gao, K. Rao, E. Morosan, K. Kindo, T. Masuda, K. Hashimoto, T. Shibauchi and P. Dai, Anomalous Electrical Transport in the Kagome Magnet $YbFe_6Ge_6$, *Phys. Rev. Lett.*, 2025, **134**, 186501.

14 J. M. Cadogan and D. H. Ryan, A Study on the Magnetic Behaviour of Polymorphic $YbFe_6Ge_6$, *J. Phys.: Condens. Matter*, 2010, **22**, 016009.

15 R. Meduri, M. A. Plata, G. T. McCandless, B. C. Schundelmier, M. Ghafoor, K. Wei and J. Y. Chan, Evolution of Structural Order and Magnetic Anisotropy in $Yb_{0.5}(Co_{1−x}Fe_x)_3Ge_3$ through Doping of a Kagome Lattice, *Chem. Mater.*, 2025, **37**, 2302–2313.

16 D. C. Fredrickson, S. Lidin, G. Venturini, B. Malaman and J. Christensen, Origins of Superstructure Ordering and Incommensurability in Stuffed CoSn-Type Phases, *J. Am. Chem. Soc.*, 2008, **130**, 8195–8214.

17 B. C. El Idrissi, G. Venturini and B. Malaman, Crystal Structures of RFe_6Sn_6 (R = Sc, Y, Gd-Tm, Lu) Rare-Earth Iron Stannides, *Mater. Res. Bull.*, 1991, **26**, 1331–1338.

18 X. Wu, X. Mi, L. Zhang, C.-W. Wang, N. Maraytta, X. Zhou, M. He, M. Merz, Y. Chai and A. Wang, Annealing-Tunable Charge Density Wave in the Magnetic Kagome Material FeGe, *Phys. Rev. Lett.*, 2024, **132**, 256501.

19 M. E. Fieser, M. G. Ferrier, J. Su, E. Batista, S. K. Cary, J. W. Engle, W. J. Evans, J. S. Lezama Pacheco, S. A. Kozimor, A. C. Olson, A. J. Ryan, B. W. Stein, G. L. Wagner, D. H. Woen, T. Vitova and P. Yang, Evaluating the electronic structure of formal LnII ions in $LnII(C_5H_4SiMe_3)_3^{1−}$ using XANES spectroscopy and DFT calculations, *Chem. Sci.*, 2017, **8**, 6076–6091.

20 J. Yamaguchi, A. Sekiyama, S. Imada, H. Fujiwara, M. Yano, T. Miyamachi, G. Funabashi, M. Obara, A. Higashiya, K. Tamasaku, M. Yabashi, T. Ishikawa, F. Iga, T. Takabatake and S. Suga, Kondo Lattice Effects and the Collapse of Lattice Coherence in $Yb_{1−x}Lu_xB_{12}$ Studied by Hard X-ray Photoelectron Spectroscopy, *Phys. Rev. B: Condens. Matter Mater. Phys.*, 2009, **79**, 125121.

21 M. Okawa, M. Matsunami, K. Ishizaka, R. Eguchi, M. Taguchi, A. Chainani, Y. Takata, M. Yabashi, K. Tamasaku, Y. Nishino, T. Ishikawa, K. Kuga, N. Horie, S. Nakatsuji and S. Shin, Strong Valence Fluctuation in the Quantum Critical Heavy Fermion Superconductor ß-$YbAlB_4$ A Hard X-Ray Photoemission Study, *Phys. Rev. Lett.*, 2010, **104**, 247201.

22 Y. Utsumi, H. Sato, S. Ohara, T. Yamashita, K. Mimura, S. Motonami, K. Shimada, S. Ueda, K. Kobayashi, H. Yamaoka, N. Tsujii, N. Hiraoka, H. Namatame and M. Taniguchi, Electronic Structure of Kondo Lattice Compounds $YbNi_3X_9$ (X = Al, Ga) Studied by Hard X-ray Spectroscopy, *Phys. Rev. B: Condens. Matter Mater. Phys.*, 2012, **86**, 115114.

23 A. He, E. L. K. Wille, L. M. Moreau, S. M. Thomas, J. M. Lawrence, E. D. Bauer, C. H. Booth and S. M. Kauzlarich, Intermediate Yb Valence in the Zintl Phases $Yb_{14}MSb_{11}$ (M = Zn, Mn, Mg): XANES, Magnetism, and Heat Capacity, *Phys. Rev. Mater.*, 2020, **4**, 114407.

24 D. H. Ryan and J. M. Cadogan, Observation of Independent Iron and Rare-Earth Ordering in RFe_6Ge_6 (R = Y, Gd–Lu) Compounds, *J. Appl. Phys.*, 1996, **79**, 6004–6006.

25 D. H. Ryan, J. M. Cadogan and R. Gagnon, The Spin-Reorientation Transition in H-type $YbFe_6Ge_6$, *J. Phys.: Conf. Ser.*, 2010, **217**, 012124.

26 CCDC 2528289: Experimental Crystal Structure Determination, 2026, DOI: 10.25505/fiz.icsd.cc2qvwq6.